Generation of global 1 km all-weather instantaneous and daily mean land surface temperature from MODIS data

Bing Li[1], Shunlin Liang[2], Han Ma[2], Xiaobang Liu[3], Tao He[4], Yufang Zhang[5]

[1] Key Research Institute of Yellow River Civilization and Sustainable Development & Collaborative Innovation Center on Yellow River Civilization of Henan Province, Henan University, Kaifeng, 475001, China

[2] Department of Geography, University of Hong Kong, Hong Kong 999077, China

[3] The 27th Research Institute of China Electronics Technology Group Corporation, Zhengzhou 450047, China

[4] School of Remote Sensing and Information Engineering, Wuhan University, Wuhan 430079, China

[5] School of Software, Northwestern Polytechnical University, Xi'an 710072, China

Correspondence to: Shunlin Liang (shunlin@hku.hk)

Abstract: Land surface temperature (LST) serves as a crucial variable in characterizing climatological, agricultural, ecological, and hydrological processes. Thermal infrared (TIR) remote sensing provides high temporal and spatial resolution for obtaining LST information. Nevertheless, TIR-based satellite-LST products frequently exhibit missing values due to cloud interference. Prior research on estimating all-weather instantaneous LST has predominantly concentrated on regional or continental scales. This study involved generating a global all-weather instantaneous and daily mean LST product spanning from 2000 to 2020 using XGBOOST. Multisource data, including Moderate-Resolution Imaging Spectroradiometer (MODIS) top-of-atmosphere (TOA) observations, surface radiation products, and reanalysis data, were employed. Validation using an independent dataset of 77 individual stations demonstrated the high accuracy of our products, yielding RMSEs of 2.787 K (instantaneous) and 2.175 K (daily). The RMSE for clear-sky conditions was 2.614 K

26   for the instantaneous product, slightly lower than the cloudy-sky RMSE of 2.931 K. Our

27   instantaneous and daily mean LST products exhibit higher accuracy compared to the MODIS

28   official LST product (RMSE=3.583 K instantaneous, 3.105 K daily) and the land component of the

29   5th generation of European ReAnalysis (ERA5-Land) LST product (RMSE= 4.048 K instantaneous,

30   2.988 K daily). Significant improvements are observed in our LST product, notably at high latitudes,

31   compared to the official MODIS LST product. The LST dataset from 2000 to 2020 at the monthly

32   scale, the daily mean LST on the first day of 2010 can be freely downloaded from

33   https://doi.org/10.5281/zenodo.4292068(Li et al. 2024), and the complete product will be available

34   at https://glass-product.bnu.edu.cn/dload.html.

35

36   **Keywords: land surface temperature, all-weather, global, XGBOOST, MODIS**

1 Introduction:

Land surface temperature (LST) is the skin temperature of the Earth's surface, and one of the crucial parameters in the surface energy balance, and the hydrothermal cycle (Bastiaanssen et al. 1998; Tomlinson et al. 2011). LSTs retrieval from in situ measurements or satellites are widely used in many scientific fields (Kappas and Phan 2018), such as climate change (Weng 2009), urban heat island (Zhou et al. 2018), drought monitoring (Wan et al. 2010), longwave radiation estimation (Cheng and Liang 2016), evapotranspiration (Kalma et al. 2008; Yao et al. 2012), soil moisture estimation (Zhang et al. 2015), and air temperature estimation (Chen et al. 2021; Rao et al. 2019; Shen et al. 2020). High-precision measurements of LST aid in the recording of the long-term global temperature trends, thus, the International Geosphere and Biosphere Programme (IGBP) lists it as one of its priority parameters (Townshend et al. 2007). Owing to the complex and rapid variation in temporal and spatial scales, in situ measurements cannot provide regional LST or capture the spatial variation in LST. Remote sensing has become the only way to obtain LST with high spatial and temporal resolution from regional to global scales (Li et al. 2013).

Over the past few decades, substantial advancements have been made in the inversion of LST from remote sensing satellites. The retrieval of satellite LST products is predominantly accomplished using thermal infrared (TIR) remote sensing data(Li et al. 2013). These LST products typically exhibit a notable spatial resolution, exemplified by the Visible Infrared Imaging Radiometer Suite (VIIRS) boasting a resolution of 750 meters, and the Moderate-Resolution Imaging Spectroradiometer (MODIS) satellite with a resolution of 1 kilometer(Wan 2014; Wan and Li 1997). Nevertheless, due to the constrained penetration capability of thermal radiation, TIR data is exclusively applicable for observing LST under clear-sky conditions. Global average annual cloud coverage has been reported to exceeds 70% (Mercury et al. 2012). The lack of data has significantly constrained the application of LST products. Consequently, estimation of all-weather LST is one of the difficulties that needs to be solved urgently.

Besides data gaps due to cloud contamination, extending the temporal scale of LST poses a significant challenge in retrieving LST products through remote sensing, requiring urgent attention. LST, a dynamic physical attribute, exhibits temporal variation. However, satellite-derived LST captures only instantaneous observations at specific times and angles. Instead of focusing solely on instantaneous LST, certain researchers emphasize the importance of daily, monthly, or yearly average LST to track the impact of increasing LST on glaciers, ice sheets, and vegetation within the Earth's ecosystem(Lawrimore et al.

67   2011). According to our current understanding, examining MODIS LST products, there exist daily

68   instantaneous L2 products, daily gridded instantaneous L3 products, and eight-day synthetic products

69   (Wan 2014). Nevertheless, there's an absence of L4 products encompassing daily mean, monthly, and

70   annual LST data. Hence, it holds significant importance to estimate daily mean LST based on limited

71   MODIS observations. Acquiring the daily mean LST allows estimation of monthly or annual mean LST,

72   crucial for prolonged monitoring across diverse research domains like climate change, agriculture, and

73   drought studies.

74   As for filling LST gaps under cloudy-sky conditions, researchers have explored various methods.

75   One type of approach is based on space-time information, such as interpolation and fusion methods (Pede

76   and Mountrakis 2018). Interpolation methods usually utilize temporally or spatially proximate clear-sky

77   pixel information to fill in the pixels under the cloudy-sky condition. Nevertheless, the efficacy of the

78   interpolation method is contingent upon the accessibility of clear-sky pixels. The reconstruction

79   outcomes prove less satisfactory in instances of extensive missing regions or prolonged periods of cloud

80   cover (Metz et al. 2014; Zhang et al. 2018; Zhang et al. 2022). In recent years, spatiotemporal fusion

81   methods have been explored for obtaining all-weather LST(Chen et al. 2015; Long et al. 2020; Wu et al.

82   2019). The essence of spatiotemporal fusion for LST involves deriving high spatial resolution LST at

83   time t0 from its counterpart with coarse spatial resolution at the identical time instance, achieved through

84   the application of a scale conversion factor (Long et al. 2020; Wu et al. 2019). Due to the algorithm's

85   complexity, fusion methods are commonly evaluated within limited geographical scopes, with their

86   applicability constrained when extended to larger areas. Furthermore, both interpolation and

87   spatiotemporal fusion methods hinge on information derived from clear-sky pixels, yielding

88   reconstructed theoretical clear-sky LST rather than the real cloudy-sky LST. In order to obtain actual

89   LST under cloudy-sky conditions, one type of approach takes into account of the physical processes of

90   the surface energy balance (SEB) (Jia et al. 2021; Jin and Dickinson 2000; Yu et al. 2014). Jin and

91   Dickinson (2000) introduced a method utilizing SEB to account for changes in solar radiation on LST

92   during cloudy conditions. This approach corrects clear-sky LST using the SEB equation to derive actual

93   cloudy-sky LST. Over time, the SEB-based method has been refined for geostationary Meteosat Second

94   Generation (Lu et al. 2011) and MODIS data (Yu et al. 2014; Zeng et al. 2018). However, widespread

95   application is limited due to gaps in data coverage and the necessity of meteorological SEB parameters

96   (e.g., air temperature, wind speed), which are challenging to obtain at regional and global scales.

97   Apart from the mentioned methods for getting LST under cloudy-sky conditions, alternative

98   approaches utilize all-weather data like microwave data, reanalysis data, or model simulations to derive

99   the cloudy-sky information. Passive microwave (PMW) data are less affected by cloud contamination,

100   which provide a possibility for all-weather LST estimations (De Jeu 2003; Duan et al. 2017b; Holmes et

101   al. 2009). However, the existing microwave observations usually have coarse resolutions (e.g., AMSR-

102   E with 25km) (Mao et al. 2007). Due to the land surface microwave emissivity is sensitive to land surface

103   characteristics and is difficult to measure, the accuracy of the PMW LST data is relatively lower than

104   that of TIR LST(McFarland et al. 1990).In addition, PMW data basically all have swath gaps, especially

105   at low latitudes, which makes it difficult to obtain full-coverage LST (Holmes et al. 2009; Zhou et al.

106   2015). Thus, LST retrieval from PMW data cannot satisfy the requirements of high-precision and refined

107   applications. Some scholars have explored the possibility of combining PMW and TIR data to estimate

108   all-weather LST (Duan et al. 2017b; Wu et al. 2022; Xu and Cheng 2021; Zhang et al. 2020). These

109   methods perform well at regional or national scales. However, owing to the availability of PMW data

110   and the complexity of algorithms, it is difficult to achieve long-term production at global scale.

111   In comparison, reanalysis data can provide another way for all-weather LST estimation, with all-

112   weather observations, long-term and seamless characteristics. With the updating of reanalysis and

113   modeled data, spatial resolution and accuracy are improved (Muñoz-Sabater et al. 2021). Recently,

114   several studies have attempt to utilizing reanalysis data combining with TIR (Long et al. 2020; Zhang et

115   al. 2021) and PMW data (Zhang et al. 2020) to obtain all-weather LST. Researchers have a growing

116   interest in estimation of all-weather LST at the global scale. Shiff et al. (2021) integrated modeled

117   temperature data to supplement missing values in MODIS LST using the Google Earth Engine (GEE).

118   Nevertheless, the proposed approach solely addressed missing pixels, potentially introducing border

119   effects. Globally, continuous spatiotemporal LST data at a resolution of 0.05° have been generated,

120   rectifying reconstructed missing data under cloudy-sky conditions using reanalysis data (Yu et al. 2022) .

121   Additionally, global seamless 8-day and monthly average LST data, featuring a 30 arcsecond resolution,

122   were created by integrating reanalysis data(Yao et al. 2023). These studies confirm the potential of

123   reanalysis data for estimating all-weather LST, yet there remains ample room for exploration at a

124   spatiotemporal scale of one kilometer per day.

125   Regarding daily mean LST, researchers have investigated acquiring it from polar-orbiting satellites.

126   Specifically, they have employed MODIS instantaneous LSTs to estimate the daily mean

127   LST(Williamson et al. 2014; Xing et al. 2021). The maximum-minimum method determined the daily

128   mean LST by averaging its maximum and minimum values, exhibiting a strong correlation with surface

129   air temperature (Williamson et al. 2014). Despite its relatively low accuracy, it presents a straightforward

130   means of estimating daily mean LST using the limited observations from polar orbiting satellites.

131   Another approach involves the diurnal temperature cycle (DTC), employing various nonlinear models

132   based on heat conduction and energy balance equations(Aires et al. 2004; Duan et al. 2012; Inamdar et

133   al. 2008; Sun and Pinker 2005), capable of retrieving daily mean LST. However, the DTC method

134   requires specific satellite observation counts within the daily cycle, posing challenges for estimating all-

135   weather daily mean LST, especially for polar-orbiting satellites with restricted observations and cloud

136   contaminants. Hong et al. (2021) proposed a framework combining the annual temperature cycle (ATC)

137   and DTC to retrieve all-weather daily mean LST at a spatial resolution of 0.5°×0.5° (Hong et al. 2022).

138   Xing et al. (2021) utilized global in situ measurements and multiple linear regression to enhance the

139   MODIS satellite's daily mean LST model accuracy, specifically under clear-sky conditions, leveraging

140   increased observations within a daily cycle. Additionally, Li et al. (2023) integrated pre-2000 polar-

141   orbiting satellite data to improve the global daily mean LST model. Most methods are applicable

142   exclusively under clear-sky conditions, and the relationship between daily mean LST and instantaneous

143   observations may not always align with cosine or multiple linear equations. Limited studies have

144   estimated daily mean LST from polar-orbiting satellites due to their restricted observations. Currently,

145   no research has estimated daily mean LST using MODIS data in swath type with enhanced observations,

146   potentially improving accuracy. Few studies have explored all-weather daily mean LST, particularly at a

147   global scale with a 1 km spatial resolution. Obtaining all-weather daily mean LST from polar-orbiting

148   satellite observations (e.g., MODIS) remains a significant challenge.

149   Recently, machine learning and deep learning techniques have gained significant traction in remote

150   sensing due to their superior model fitting capabilities(Ma et al. 2019; Yuan et al. 2020). Scholars have

151   investigated LST retrieval using learning techniques across various satellite platforms (Li et al. 2021;

152   Mao et al. 2018; Wang et al. 2010). However, the majority of these methods utilized clear-sky pixels as

153   the true value to construct the model, possibly failing to capture the relationship under cloudy-sky

154 conditions. Additionally, learning methods have not yet been applied for estimating daily mean LST. Our

155 former research has estimated all-weather LST from MODIS data using a random forest over the

156 conterminous United States (Li et al. 2021). This study refined our previously developed algorithm for

157 an all-weather instantaneous LST product and developed a new method for a daily mean LST product at

158 a global scale. The improvements over our previous study (Li, et al., 2021) include: 1) MODIS top-of-

159 atmosphere (TOA) information was also taken into account; 2) a novel algorithm was proposed to

160 estimate daily mean LST from multiple MODIS observations; and 3) a higher efficiency learning

161 algorithm was used to generate the all-weather LST products at global scale.

162 The rest of the paper is organized as follows. Section 2 describes the data used in this paper. Section

163 3 provides a summary of the proposed method. The results are presented in Section 4. A discussion part

164 is presented in Section 5. Section 6 is the data availability. Finally, Section 7 presents the conclusions.

165

166 **2 Data**

167 **2.1 Remotely sensed data**

168 The remote sensing data used in this study are summarized in Table 1. MOD021KM and

169 MYD021KM are MODIS TOA observational datasets. The shortwave bands (B1–B7, B19) and

170 longwave bands (B27–B36) were selected as model inputs. Geolocation information was obtained from

171 MODIS geolocation data (MOD03 and MYD03). The coordinates from MODIS geolocation data were

172 used to match up with products and in situ measurements, while height, solar zenith angle, solar azimuth

173 angle, view zenith angle and view azimuth angle were used as the model inputs. MODIS LST

174 (MOD11L2/MYD11L2) was used for the comparison and identification of cloudy-sky conditions.

175 MODIS data were derived from https://earthdata.nasa.gov/. The Global LAnd Surface Satellite (GLASS)

176 product suite includes at least 12 land surface variables, which have high spatial resolutions (1 km and

177 0.05°), long-term temporal coverage (1981– present), spatial continuity, and high quality (Liang et al.

178 2021; Liang et al. 2013a; Liang et al. 2013b). In this study, we used the following four products from the

179 GLASS product suite: Broad band emissivity (BBE), broadband albedo (albedo), downward solar

180 radiation (DSR), and downward thermal radiation (LWDN). BBE product was used to obtain in-situ LST

181 (Cheng and Liang 2013, 2014). Albedo was used as the model input to describe surface characteristics

182 (Liu et al. 2013a; Qu et al. 2016; Qu et al. 2014). Because LST is affected by both solar radiation and

183 surface longwave radiation, DSR and LWDN were also used in the model construction (Cheng et al.

184 2017; Zhang et al. 2019).

185 Table 1. Summary of remote sensing data

| Product	Variables	Resolution (temporal /spatial)	Usage
MOD021KM /MYD021KM	Toa reflectance, brightness temperature	Instantaneous/1 km	Model inputs
MOD03/MYD03	Latitude, longitude, height,	Instantaneous/1 km	Model inputs/match up
MOD11L2/MYD11L2	LST	Instantaneous/1 km	Comparison
GLASS	BBE	8 days/1km	Calculate in situ LSTs
GLASS	Albedo	8 days/1km	Model inputs
GLASS	DSR	Daily/0.05°	Model inputs
GLASS	LWDN	Instantaneous/1 km	Model inputs

186   **2.2 Reanalysis data**

187   In recent years, an enhanced global dataset for the land component of the fifth generation of

188   European ReAnalysis (ERA5-Land) has been developed (Hersbach et al. 2020; Muñoz-Sabater et al.

189   2021). ERA5-Land describes a consistent long terms evolution of water and energy cycles over land. It

190   was generated through global high-resolution numerical integrations of the European Centre for

191   Medium-Range Weather Forecasts (ECMWF) land surface model driven by the downscaled

192   meteorological forcing from the ERA5 climate reanalysis. Compared with the previous ERA-Interim (80

193   km) and ERA (31 km), ERA5-Land has a higher spatial resolution (9 km) and temporal resolution (1 h).

194   Because ERA5-Land LST includes worldwide and all-weather data, it was used in the model construction

195   as the background value and was also used for comparison. ERA5-Land LST is hereafter referred to as

196   ERA LST.

197   **2.3 In situ measurements**

198   To obtain in situ LSTs, we collected upwelling and downwelling longwave radiation measurements

199   from 315 sites with different land cover types and geolocations on a global scale. Both instantaneous and

200   daily mean in situ LSTs were retrieved from in situ measurements. As shown in Fig. 1, ground

201   measurements from 238 stations were used to develop the proposed network (blue circles), whereas the

202   measurements from the remaining 77 stations (red circles) were selected as independent validation

203   datasets to evaluate the performance of the trained model. The collection sites were mainly from eight

204   observation networks, which are described in the following paragraphs.
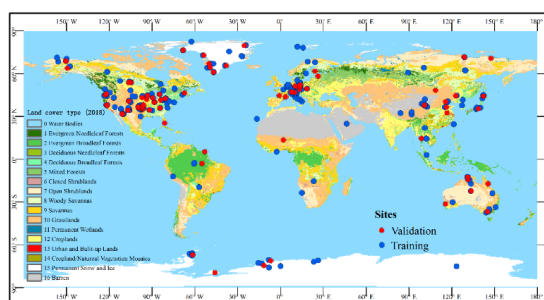
205

206   Fig. 1 Spatial distribution of the selected sites at a global scale. Land use cover types of 2018 (background color shading) were

207   from the MODIS land use cover product MCD12C1. The site used for model training are shown with blue circles while the

208   separated validation sites are shown with red circles.

209

210   AmeriFlux (https://ameriflux.lbl.gov/) is a network of stations that continuously measures
211   ecosystem carbon dioxide, water, energy fluxes, and related environmental variables using eddy
212   covariance techniques (Baldocchi 2003). The network was launched in 1996, and was established to
213   connect research on field sites representing major climate and ecological biomes(Boden et al. 2013). The
214   network has more than past and present flux towers, and sites with longwave radiation measurements
215   were selected. These sites are distributed across North, Central, and South America. The observation
216   interval of these sites was half an hour.

217   FLUXNET (https://fluxnet.org/) is a global network of micrometeorological tower sites that uses
218   eddy covariance methods to measure carbon dioxide, water vapor, and energy fluxes (Baldocchi et al.
219   2001). It has more than 500 flux towers worldwide are operating on a long-term basis. The overarching
220   goal of the FLUXNET data collection is to provide information for validating remote sensing products,
221   such as net primary productivity and energy fluxes. Sites with longwave radiation records were used in
222   this study. The observation interval of the sites was half an hour.

223   The Baseline Surface Radiation Network (BSRN, https://bsrn.awi.de/) is a project of the Data and
224   Assessments Panel of the Global Energy and Water Cycle Experiment (GEWEX) under the umbrella of
225   the World Climate Research Programme (WCRP) (Ohmura et al. 1998). The purpose of this network is
226   to provide validation materials for satellite radiometry and climate models. It further aims to detect long-
227   term variations in the radiation field at the Earth's surface, which play a vital role in climate changes
228   (Driemel et al. 2018). The stations (currently 74 in total, 58 active) are distributed in contrasting climatic
229   zones, covering a latitude range from 80° N to 90° S. The required longwave radiation measurements
230   were obtained with high accuracy and high time resolution (1 – 3 minutes).

231   AsiaFlux (https://www.asiaflux.net/) is a scientific community with the aim of developing
232   collaborative research and datasets on carbon, water, and energy cycles in key Asian ecosystems.
233   AsiaFlux has grew from a small network in 1999 to a multi-national science community with more than
234   400 members from 28 countries (Yamamoto 2005). Currently, there are 109 flux towers in Asia, and
235   more sites are underway. The biomes covered in AsiaFlux range from rainforests near the equator to
236   tundra in the Arctic and Antarctic, and from wetlands near sea level to grasslands at high altitudes, such
237   as the Tibetan Plateau. Most sites have a time resolution of 0.5 hour, while 15 minutes and 1 hour are
238   used for individual sites.

239   The Atmospheric Radiation Measurement (ARM, https://www.arm.gov/) Program, supported by the

240   U.S. Department of Energy, is a project for atmospheric measurement and modeling. The purpose of the

241   project was to detect processes that affect atmospheric radiation and describe these processes in climate

242   models (Stokes and Schwartz 1994). The quantities measured at these stations included longwave and

243   shortwave radiation, clouds properties, water vapor, other radiation-related quantities, and

244   meteorological variables. These sites had the high temporal resolution of 1 minute.

245   The Ice and Climate group at the Institute for Marine and Atmospheric Research of Utrecht

246   University (UU/IMAU) (https://www.projects.science.uu.nl/iceclimate/) has deployed several Automatic

247   Weather Stations (AWS) on different glaciers around the world (Antarctica, Greenland, Alps, Norway,

248   Iceland, Svalbard), and in different climate regimes. The stations were designed to operate on a long-

249   term basis and measure meteorological and radiation variables in remote regions under harsh weather

250   conditions. The main purpose of these stations is to detect the energy balance in these regions in view of

251   climate change and, sea-level variation. The stations from the IMAU project have time resolutions of 1

252   and 2 hours.

253   Denmark launched the Programme for Monitoring of the Greenland Ice Sheet (PROMICE)

254   (https://www.promice.dk/) to detect variations in the mass balance of the Greenland ice sheet. Several

255   weather stations were established on the ice sheet to provide filed data for modeling and validation. The

256   weather stations were equipped with CNR1 or CNR4 instruments to measure radiation data with a time

257   resolution of 10 minutes.

258   The National Tibetan Plateau Data Center (TPDC) (http://data.tpdc.ac.cn) has integrated and

259   released various scientific data from the Qinghai-Tibet Plateau and surrounding regions. Integrated data

260   resources include the atmosphere, cryosphere, hydrosphere, and energy balance. Among these data

261   sources, there are various published ground measurements. We selected several stations in the Heihe

262   Basin (Liu et al. 2018), Haihe Basin (Liu et al. 2013b), and Qinghai-Tibet Plateau (Ma et al. 2020). The

263   time resolutions of these stations were 10 minutes, 30 minutes and 1 hour, respectively.

264   Some stations from various flux networks overlapped, and we curated observations with extended

265   time series and heightened time resolution. Attaining high model accuracy necessitates superior in situ

266   measurements, necessitating rigorous quality assessment. Initially, adjacent stations potentially causing

267   interference were removed, alongside the manual elimination of anomalous observations and

268   discontinuous measurements. Subsequently, the collection sites were strategically dispersed globally. Fig.

269   2 depicts a histogram illustrating the distribution of land cover types and climate zones across the sites.

270   Each land cover type was accounted for, and additional sites encompassing water bodies were

271   incorporated to estimate LST for inland water. The stations were dispersed across five distinct climate

272   zones, with a higher concentration in temperate and continental climates. Importantly, we meticulously

273   gathered data from numerous high-latitude stations within a polar climate to address substantial

274   estimation uncertainties in the area.

275
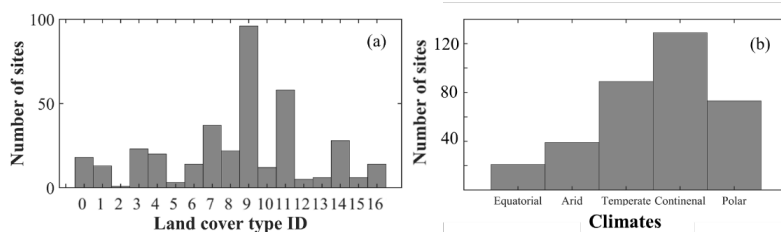
276   Fig. 2 Land cover types (a) and climate zones (b) of sites (The land surface type represented by the x-axis in

277   Fig. 2 (a) refers to the legend in Fig.1)

278

279

3 Methods

The study's comprehensive framework is depicted in Fig. 3. Initially, the in situ LST and remote sensing data underwent preprocessing and pairing. Subsequently, the data pairs were randomly divided into two segments: one for model training and validation, while the other served as an independent dataset for model evaluation. The XGBOOST algorithm was employed to sequentially develop models for instantaneous and daily mean LST, while also conducting parameter tuning. The estimated all-weather instantaneous LST served as an input for the daily mean LST model. Ultimately, the optimal models underwent separate evaluation and comparison with alternative products.
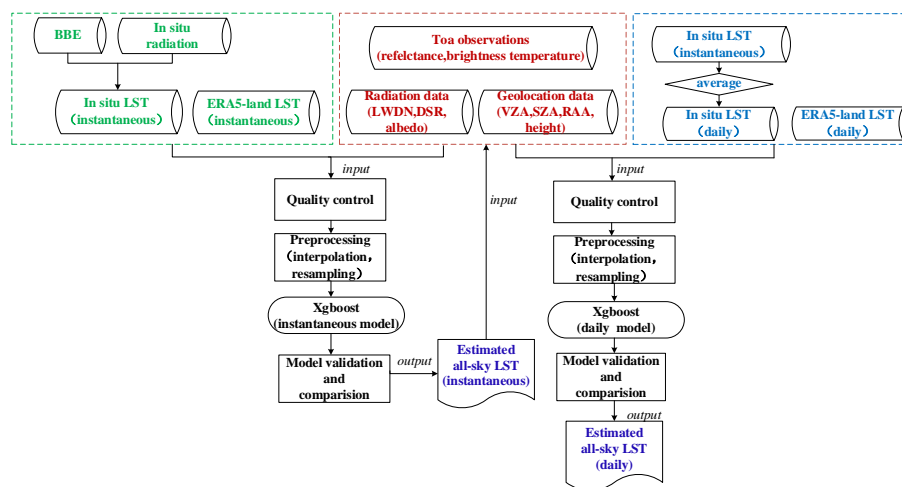

Fig. 3. Flowchart of the XGBOOST algorithm for all-weather instantaneous and daily mean LST estimation.

3.1 Data Preprocessing

3.1.1 In situ instantaneous LST

The in situ LST in this study was calculated from surface broadband emissivity and in situ upwelling and downwelling longwave radiation, according to Stefan–Boltzmann's law, as follows:

$$T_S = \left(\frac{F_{up} - (1-\varepsilon)F_{dn}}{\sigma\varepsilon}\right)^{\frac{1}{4}} , \qquad (1)$$

where T_S represents the in situ LST, F_{up} is the upwelling longwave radiation, and F_{dn} is the downwelling longwave radiation, ε is surface broadband emissivity, and σ is the Stefan-Boltzmann constant (5.67×10^{-8} W/m^2/K^4).

299   Surface broadband emissivity was acquired from the GLASS BBE product through nearest

300   interpolation to derive daily values. F_{up} and F_{dn} were derived from in situ measurements. Due to

301   varying observation intervals across different networks, spanning from 1 minute to 1 hour, a linear

302   interpolation method was applied to determine the in situ LST corresponding to the MODIS satellite

303   observation time.

304   **3.1.2 Daily mean LST**

305   To constructing a daily mean LST model, in situ daily mean LST and ERA5-land daily mean LST

306   are required. Once the instantaneous LST from in situ measurements was obtained, the daily mean in situ

307   LST was calculated according to the Eq. (2). The ERA5-land daily mean LST was obtained using Eq.

308   (3).

309   $$LST_{DS} = \frac{1}{n}\sum_{i=1}^{n} LST(i)_{IS} \tag{2}$$

310   $$LST_{DE} = \frac{1}{24}\sum_{i=1}^{24} LST(i)_{IE} \tag{3}$$

311   LST_{DS} and LST_{DE} represent the daily mean in situ LST and daily mean ERA5-land LST

312   respectively, and n is the count of the in situ measurements per day. LST_{IS} and $LST(i)_{IE}$ are the

313   instantaneous in situ LST values calculated from Eq. (1) and ERA5-land LST, respectively. If the in situ

314   measurements were incomplete in a day, the record for that day was not used.

315   One traditional daily mean LST method, which was retrieved from the official MODIS Aqua LST

316   for both daytime and nighttime (Williamson et al. 2014), was used for comparison. The equation can be

317   expressed as follows:

318   $$LST_{DM} = 0.5 * LST_{AD} + 0.5 * LST_{AN} \ , \tag{4}$$

319   where LST_{DM} represents the retrieval of the daily mean LST, and LST_{AD} and LST_{AN} represent

320   the daytime and nighttime LST, respectively from the official MODIS Aqua LST.

321

322   **3.1.3 Data normalization**

323   Due to varying spatial and temporal resolutions among the utilized products, preprocessing was

324   conducted. Albedo and BBE had an 8-day temporal resolution, and daily albedo was acquired through

325   nearest interpolation. DSR and ERA5-land LST were adjusted to a spatial resolution of 1 km via the

326 nearest-neighbor method. The ERA5-land LST, with a temporal resolution of 1 hour, was interpolated

327 linearly to obtain the reanalysis LST at the satellite observation time. Matching of in situ measurements

328 and satellite data was performed based on coordinates from MOD03/MYD03 products.

329 Due to discrepancies in spatial and temporal resolutions among the utilized data, preprocessing steps

330 were undertaken. Albedo and BBE had an 8-day temporal resolution, and daily albedo was derived via

331 nearest interpolation. DSR and ERA5-land LST were adjusted to a spatial resolution of 1 km using the

332 nearest-neighbor method. The ERA5-land LST, with a temporal resolution of 1 hour, was linearly

333 interpolated to align with the satellite observation time. In situ measurements and satellite data were

334 aligned based on MOD03/MYD03 product coordinates.

335 **3.2 Developing the estimation algorithm**

336 Extreme Gradient Boosting (XGBOOST) is an effective and scalable gradient boosting

337 implementation introduced by Chen and Guestrin (2016). It amalgamates multiple classification and

338 regression trees to create a robust learner. In regression, the initial tree is constructed based on split

339 features, followed by the creation of subsequent trees to capture residuals from the preceding ones.

340 Additional trees are iteratively generated until they meet the stopping criteria. Notably, the regression

341 trees within XGBOOST are interrelated, progressively diminishing the residuals of predictions with new

342 trees. The ultimate prediction is derived by aggregating scores from each tree.

343 In contrast to the random forest method, which also employs decision trees (Breiman 2001),

344 XGBOOST operates in parallel. Its algorithm design incorporates column blocks for parallel learning,

345 cache-aware access, and facilitates out-of-core computation, substantially boosting computational

346 efficiency. Owing to XGBOOST's notable efficiency and precision, many studies in remote sensing have

347 adopted this algorithm for regression tasks (He et al. 2021; Kim et al. 2021; Liu et al. 2021). In this

348 research, XGBOOST was implemented using the Scikit-learn package in Python. Experiments were

349 performed on a computer equipped with a 3.60 GHz CPU and 64 GB RAM, utilizing the same dataset

350 and features. Detailed hyperparameters are elucidated in Section 3.3.

351 **3.3 Model development**

352 The dataset for 2002-2018 were compiled at a global scale. Samples from 238 sites were randomly

353 chosen for model training. The remaining samples from 77 sites were used as independent dataset for the

354 model validation. The features used to construct the instantaneous LST model, included MODIS TOA

355 observations, ERA5-land LST, DSR, LWDN, albedo, and geolocation data. MODIS TOA observations

356 were used to describe the contributions of shortwave and longwave radiation to the LST, which is greatly

357 changed with solar radiation influenced by clouds. Hence, DSR was used to reflect the effect of solar

358 radiation on the LST (Zeng et al. 2018). Longwave radiation is less affected by the atmosphere, has a

359 certain penetration, and has a close correlation and interaction with the LST during the daytime and

360 nighttime. In this study, the LWDN was used to reflect the effect of thermal infrared radiation on LST.

361 LST is also influenced by land cover types, and broadband albedo was used to represent land surface

362 characteristics. In addition, geolocation information, such as solar angles, view angles and height, also

363 affects LST retrieval from satellites. All the input variables were all-weather conditions with high

364 resolution. In addition, ERA LST can provide all-weather LST, but had coarse resolution (0.1°). It was

365 considered as a background field and, provided an initial value for the model. After the instantaneous

366 model was constructed, the daily mean model was developed. Research has confirmed linear or nonlinear

367 relationships between the daily mean LST and instantaneous LSTs for polar orbiting satellites (Duan et

368 al. 2014; Xing et al. 2021). Hence, the instantaneous retrieval of all-weather LST data was used in the

369 daily LST model. In addition, the ERA daily LST rather than the ERA LST was used as the initial value

370 in the daily LST model. Except for these two variables, the inputs of the two models were the same.

371 Specifically, the daily mean LST finally retrieval from the mean of multiple observations in one day.

372 Model tuning was performed to prevent over-fitting of the models. Several hyper-parameters in

373 XGBOOST needed to be tuned, including the number of gradient boosted trees (n_estimators), maximum

374 depth of trees (Max_depth), minimum sum of weights of all observations required in a child

375 (Min_child_weight), minimum loss reduction required to make a split (gamma), fraction of observations

376 to be randomly samples for each tree (subsample), fraction of columns to be randomly sampled for each

377 tree (Colsample_bytree). Lambda and alpha represent the regularization of the weights in XGBOOST,

378 which can improve the speed performance. A random search combined grid search was used to tune the

379 model. Table 2 presents the candidate values of the random search and the final settings for the two LST

380 models.

381

382

383   Table 2. Candidate values and selected values of hyper-parameters in XGBOOST

Hpyer-parameter	Candidate values	Selected values	
	(start, end, stride)	Instantaneous model	Daily model
n_estimators	50,401,10	160	140
Max_depth	1,10,1	9	9
Min_child_weight	1,10,1	5	6
gamma	0,1,0.1	0.8	0.5
subsample	0.1,1,0.1	1	1
Colsample_bytree	0.1,1,0.1	0.8	0.8
lambda	0.1, 2, 0.1	0.6	1.4
alpha	0.1, 2, 0.1	1.6	1.19

384

3.4 Evaluation approaches

386   In this study, validation from training and independent datasets of separated ground measurements

387 was used to evaluate the instantaneous and daily mean LST models. A widely us ed ten-fold cross

388 validation (10-CV) method was used to evaluate the stability of the models. Then, model performance

389 was assessed for different weather conditions, and observation times. In addition, time series of

390 individual sites and spatial distribution at regional and global scales were chosen to further demonstrate

391 the effectiveness of the developed models. Finally, the proposed framework and generated products were

392 compared with those of previous studies and products.

4 Results

4.1 Model training and validation

393

394

395   In general, 70% of the training dataset was used for the model training. The remaining dataset was

396   used for model adjustment and validation, and was identified as training result. Independent validation

397   and 10-CV results were used to evaluate the models. Fig. 4 and Fig. 5 show the accuracies of the

398   instantaneous and daily mean LST models, respectively. From the density plots, all the validation results

399   for both the instantaneous and daily models were close to the 1:1 line, with R^2 values range from 0.974

400   to 0.990. The Root Mean Squared Error (RMSE) of the training and validation results were 2.413 K and

401   2.787 K for the instantaneous model, and while 1.758 K and 2.175 K for the daily mean LST model.

402   Both models showed high accuracy in model training and validation, with no obvious over fitting. The

403   10-CV method was also used to comprehensively validate the models and the results of both models

404   were also satisfactory, with RMSEs =2.421 K and 1.808 K for the instantaneous and daily mean LST

405   models, respectively. Overall, the validations from the independent dataset and 10-CV results show

406   acceptable accuracy and robustness of the two models. Both models are robust. The daily mean LST

407   model showed a higher accuracy than the instantaneous LST model. Probably because the daily mean

408   LST was obtained by averaging multiple observations in one day, which reduced the uncertainty. In

409   addition, some daily inputs (daily mean in -situ LST and ERA LST) used in the daily model have less

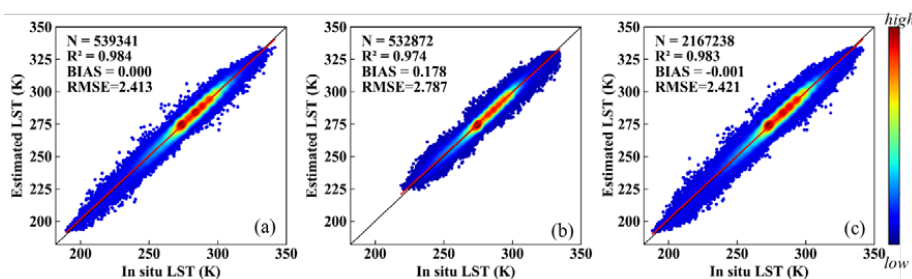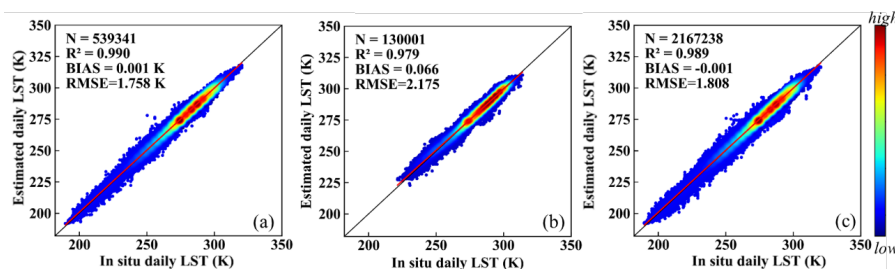410   uncertainty than instantaneous observations.

411

412   Fig. 4. The (a) training, (b) independent validation and (c) 10-CV results of the instantaneous LST model

413

414

Fig. 5 The (a) training, (b) independent validation and (c) 10-CV results of the daily mean LST model

415

416   In addition, we further verified the model performance under different conditions using an

417   independent dataset. Table 3 presents the validation results for different observation times and satellites

418   for the instantaneous model. The RMSEs were 3.03 and 2.67 K for daytime and nighttime data

419   respectively. The accuracy of nighttime data was higher than that of daytime data. It probably because of

420   the absence of differential solar heating. In addition, the LST value during the daytime was higher than

421   that during nighttime, which resulted in a higher RMSE value. For the validation of the MOD and MYD

422   satellites, the RMSE of the MOD is nearest to that of the MYD. We further verified the accuracy in the

423   presence and absence of clouds; the density plots are shown in Fig. 6. The accuracy under clear-sky

424   conditions was relatively higher with an RMSE= 2.614 K, whereas the RMSE was 2.931 K under cloudy-

425   sky conditions. More effective observation information and higher accuracy of inputs under clear-sky

426   conditions, resulted in a higher accuracy of clear-sky estimation. Furthermore, to explore whether clouds

427   have an effect on daily mean LST retrieval, we calculated the accuracy under different cloud proportions,

428   as shown in Table 3. The results showed that with the RMSE values increased slightly as the proportion

429   of cloudy-sky observations increased. This demonstrates that the cloud contamination had a limited

430   impact on the daily mean LST estimation in the proposed method.

431   Table 3. Validation for different observation times, satellites and weather condition of instantaneous the model, and the

432   proportion of cloudy-sky MODIS observations of the daily LST model

	Groups	R^2	RMSE	Bias
	Daytime	0.9601	2.99	0.30
Instantaneous LST model	Nighttime	0.9801	2.61	0.05
	MOD	0.9801	2.80	0.19
	MYD	0.9801	2.82	0.17
Daily LST model	0-30	0.9801	2.01	-0.07

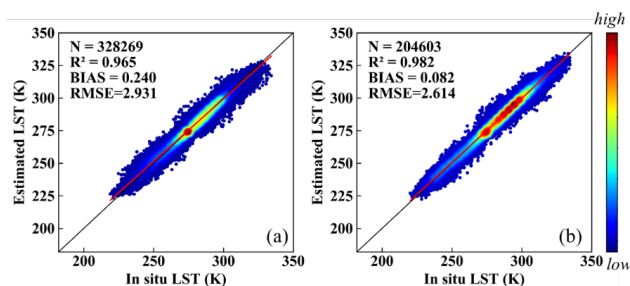|				
(Proportion of cloudy	30-60	0.9801	2.14	-0.16
MODIS observations %)	60-100	0.9801	2.26	-0.04

Fig. 6   Validation under (a) cloudy-sky condition and (b) clear-sky conditions

4.2 Validation and assessment

4.2.1 Evaluation across individual sites

The validation of the instantaneous and daily mean LST for individual sites is shown in Fig. 7. The color of the circles indicates the increasing level of errors. RMSEs rank from 1.16 to 4.90 K for instantaneous LST and 0.89 to 3.96 K for daily mean LST. The corresponding histograms show that the accuracy of nearly 75% of sites is below 3 K and 2.5 K for instantaneous and daily mean LST, respectively. Stations distributed in the continental United States with intensive LST monitoring generally have higher accuracy. High accuracy was also observed at stations in Alaska and Greenland, whereas a relatively lower accuracy was observed in the Antarctic. In Europe, most stations perform well, with the exception of some stations in the east. The stations in Asia are relatively discrete with relatively lower accuracy for individual sites in western China, which is probably due to the high elevation and complex terrain. In addition, several stations distributed in Australia, Africa, and South America also performed well in both models. In general, the results indicated a satisfactory predictive ability of both instantaneous and daily mean LST models at most individual sites.
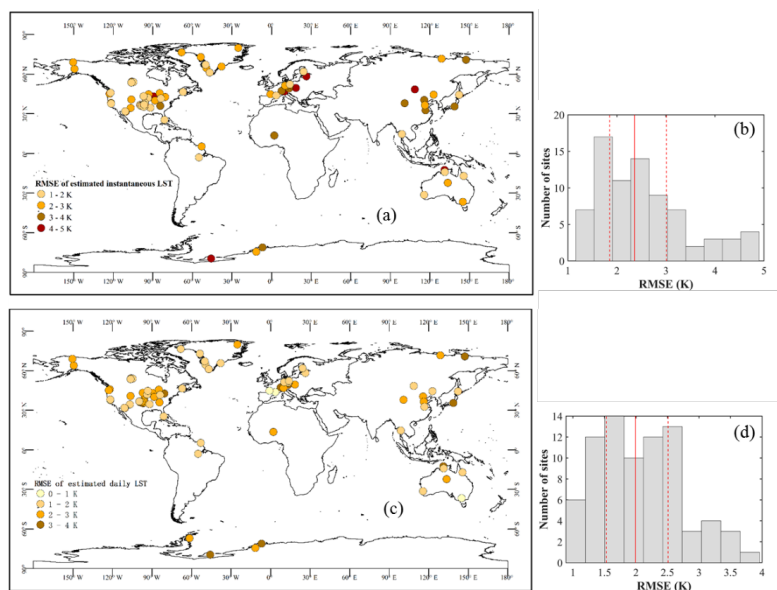
Fig. 7. Validation of individual sites for instantaneous LST (a), daily mean LST (c) and their corresponding histograms (b, d)

4.2.2 Evaluation across land cover types and elevation

LST is closely related to land cover types. The validation results for different land cover types are presented in Table 4. The results indicated that the data had high accuracies for most land cover types. For instantaneous LST, the RMSEs of most vegetation types were below 3 K, except for shrublands with an RMSE of 3.04 K. Among the vegetation types, cropland had an outstanding RMSE of 2.55 K. The accuracies of vegetation types for daily mean LST were higher than that of instantaneous LST, with RMSEs of approximately 2 K, except for shrublands with an RMSE of 2.55 K. The accuracy in water bodies was also satisfactory, with RMSEs of 2.43 and 2.04 K for instantaneous and daily mean LST, respectively. For both models, the accuracy of instantaneous and daily mean LST in snow/ice with RMSE of 2.94 and 2.35 K, respectively were notably improved compared with that found in our previous study (Li et al. 2021). This is probably due to the higher number of samples from high latitudes, which improved the model robustness in snow/ice. However, the accuracy for urban and barren areas was relatively low. This is likely due to the high heterogeneity of urban areas, high albedo and low specific heat capacity of barren land (Duan et al. 2017a). In general, for different land cover types, the daily mean model showed higher accuracy than the instantaneous model, and both models had acceptable accuracy. In addition, we summarized the accuracy of the different elevation ranges in Table 5. The results indicate

21

468 that elevation has an impact on LST retrieval accuracy. The relatively poor accuracy at high elevations

469 is probably due to the harsh natural environment and complex terrain, which was also reflected in another

470 study (Zhao et al. 2019).

471 Table 4. Validation of instantaneous and daily LST models for various land cover types

	Instantaneous LST model			Daily mean LST model		
	R^2	RMSE	Bias	R^2	RMSE	Bias
Forest	0.9409	2.82	0.11	0.9604	2.08	-0.11
Shrublands	0.9801	3.04	-1.05	0.9801	2.55	-0.85
Savannas	0.9604	2.74	0.12	0.9801	2.13	0.24
Grassland	0.9604	2.65	0.12	0.9604	2.02	0.06
Wetland	0.9801	2.87	-0.86	0.9801	2.19	-0.35
Cropland	0.9604	2.55	-0.05	0.9604	2.22	0.06
Urban	0.7744	3.76	0.4	0.8836	2.51	-0.44
Snow	0.9409	2.94	0.77	0.9604	2.35	0.69
Barren	0.9409	3.8	0.95	0.9604	3.53	0.85
Water	0.9604	2.43	-0.34	0.9801	2.04	-0.22

472 Table 5. Validation of the instantaneous and daily mean LST models for different elevations

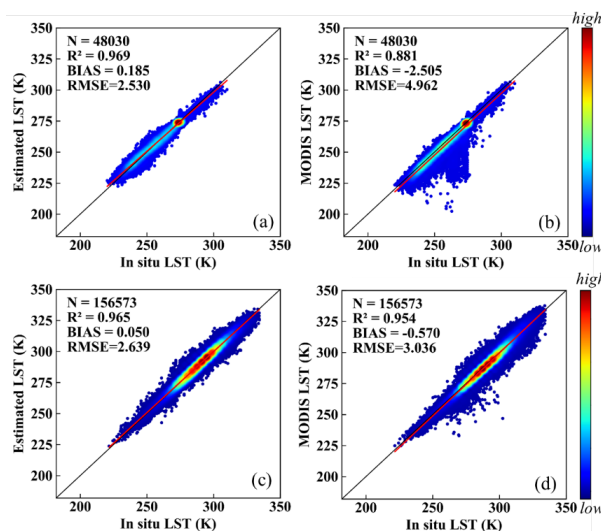|	Instantaneous LST			Daily mean LST		
Elevation (m)	R^2	RMSE (K)	Bias (K)	R^2	RMSE (K)	Bias (K)
<500	0.9604	2.63	-0.06	0.9801	2.14	0.12
500-1000	0.9801	2.85	0.60	0.9801	2.16	-0.35
1000-2000	0.9801	3.25	0.39	0.9801	2.29	-0.41
>2000	0.9409	3.79	-0.83	0.9409	2.74	1.23

473 **4.2.3 Comparison with other products**

474 Official MODIS and ERA LST data were used for comparison with our LST products. Fig. 9

475 presents the accuracy of ERA LST (RMSE = 4.048 K) and official MODIS LST (RMSE = 3.583 K),

476 both of which were lower than the accuracy of the estimated LST proposed in this study (RMSE = 2.787

477 K, Fig. 4). Furthermore, we noted that the official MODIS LST data had several abnormal points (Fig. 8

478 (b)). The polar regions (Antarctica and the Arctic pole) were verified separately from the other regions,

479 as shown in Fig. 9. The results indicate that the majority of outliers were from stations located in

480 Antarctica and the Arctic pole (Fig. 9.(b)), probably because of cloud contamination. Owing to the

481 spectral similarities between the ice and snow, the misjudgment of clouds leads to cloud top temperatures

482 rather than LST (Liu et al. 2010; Østby et al. 2014). In contrast, the proposed method was unaffected by

483 cloud contamination (Fig. 9(a)).
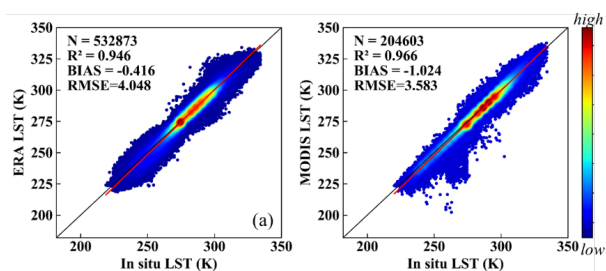
Fig. 8 Density plots of (a) ERA LST and (b) MODIS clear-sky LST

Fig. 9 Density plots of estimated instantaneous clear-sky LST (a, c) and MODIS LST (b, d) in polar regions (first row) and other regions (second row)

The daily mean LST from the ERA LST from Eq. (3), and official MODIS LST from Eq. (4)) were used for comparison (Fig. 10). The ERA daily LST had an acceptable accuracy, with an RMSE of 2.988 K. The RMSE of the daily mean official MODIS LST was 3.105 K. The accuracy of the MODIS official LST was relatively lower compared to what was reported in a previous study. This may be due to the large uncertainty in the official MODIS LST in polar regions. When removing the observations in polar regions, the accuracy improved with an RMSE of 2.799 K, similar to the result in previous studies (Williamson et al. 2014; Xing et al. 2021). The proposed method in this study has a higher accuracy than the daily mean LST from ERA and official MODIS LST, with an RMSE of 2.175 K at the global scale (Fig. 4(b)). Moreover, the daily mean LST obtained from official MODIS LST is only suitable under clear-sky conditions, whereas the daily mean LST obtained in this study was for all-weather conditions.
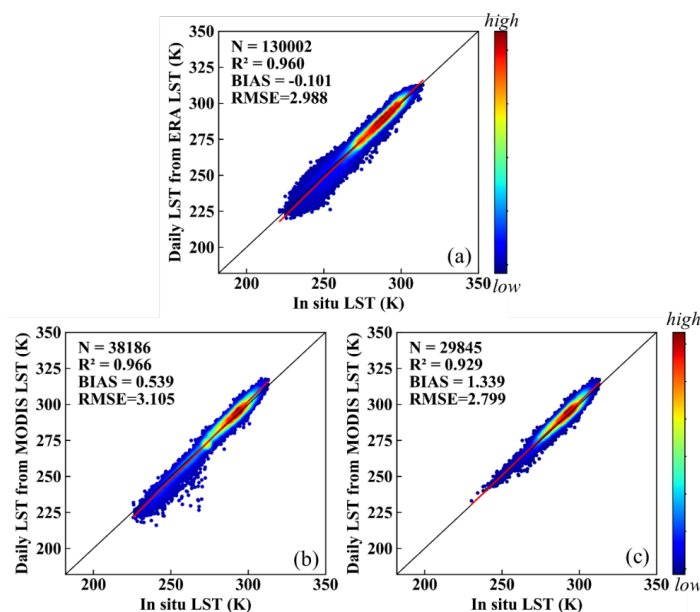
Fig. 10 Density plots of (a) ERA daily mean LST and (b) official MODIS daily mean LST

4.3 Spatiotemporal performance

To further evaluate the temporal performance of the estimated LST, four in situ LST measurements from different latitudes in 2010 were evaluated. Initially, instantaneous LST was examined separately for daytime and nighttime, and MODIS LST was provided for comparison (Fig. 11). The RMSE values of the comparable accuracy with MODIS LST. The nighttime LST was more concentrated than the daytime LST. The estimated LST curves are in good agreement with the in situ LST and MODIS LST curves, but are more continuous than the curve of MODIS LST. Discontinuities observed at high-latitudes stations (latitude:79.835, longitude: -25.166) were due to polar day and night phenomena. The daily mean LST was also examined using in situ LST measurements (Fig. 12). The daily mean LST retrieved from MODIS official LST were used for comparison. The results indicated higher accuracy and better consistency compared to instantaneous LST. The estimated daily LST also depicted more complete curves than the daily mean LST from MODIS LST, and captured the seasonal variation trends. The results demonstrate that both the estimated instantaneous LST and daily mean LST can correctly reflect the temporal variations in LST.
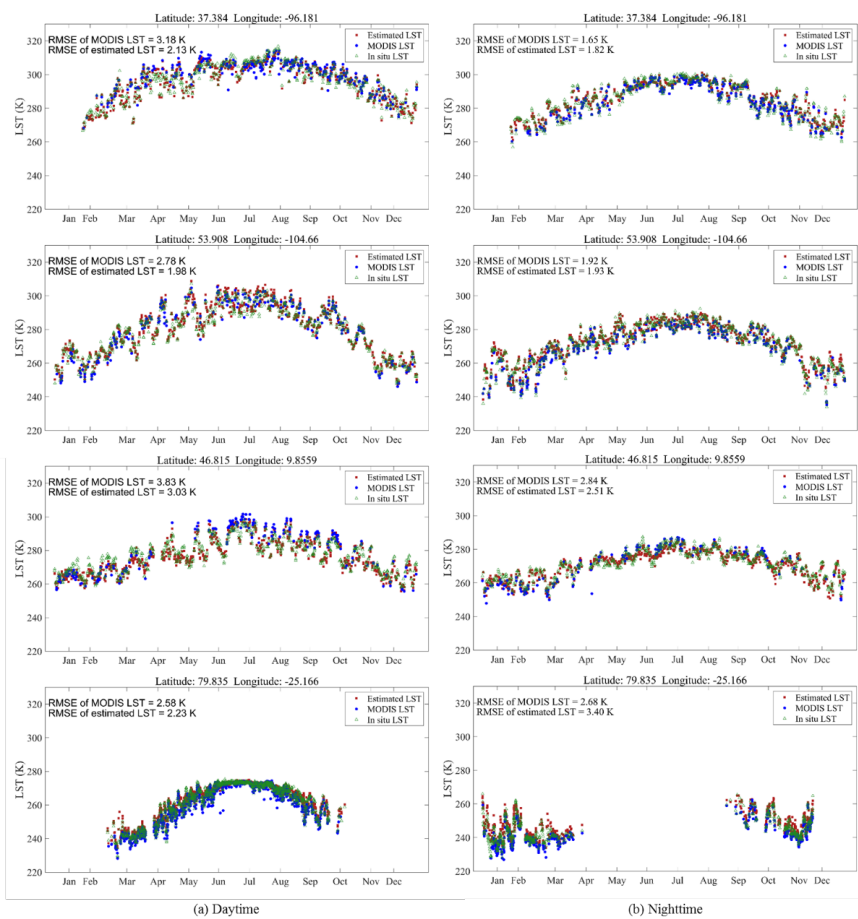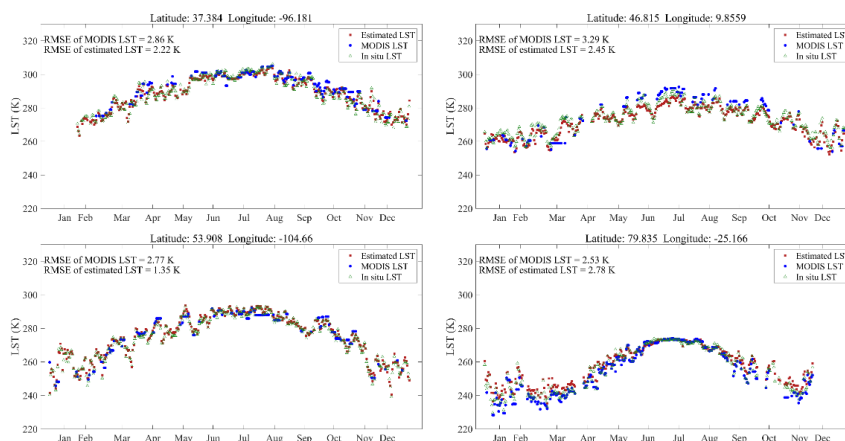
(a) Daytime (b) Nighttime

Fig. 11. Time series of the estimated instantaneous LST, MODIS LST, and in situ LST at four sites from different regions in 2010: (a) daytime, (b) nighttime.
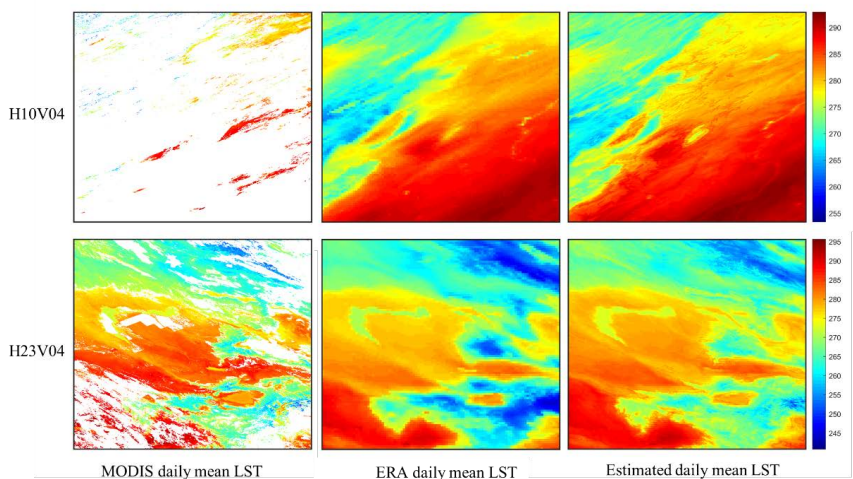
Fig. 12. Time series of the estimated daily mean LST, daily mean LST retrieved from MODIS LST, and in situ LST at four sites from different regions in 2010

To further evaluate the spatial performance of the proposed methods, regional distributions and global maps were compared. Fig. 13 and Fig. 14 present the spatial details of the estimated instantaneous LST and daily mean LST from tiles H10V04 and H23V04. The instantaneous and daily mean LST from ERA LST and MODIS LST were used for comparison. MODIS LST had missing values caused by cloud contaminants for both instantaneous and daily mean LST, while our method achieved spatially continuous estimations. In addition, the estimated LSTs had spatial patterns similar to those of MODIS LST under clear-sky conditions. Compared with the ERA LST, which was used as the model input, our results showed more spatial details and corrected the underestimation in some regions. The spatial details of the daily mean LST showed similar conclusions (Fig. 14). Overall, for both instantaneous and daily mean LST, the proposed methods executed the spatially contiguous LST and, depicted the spatial LST details and variations.

533
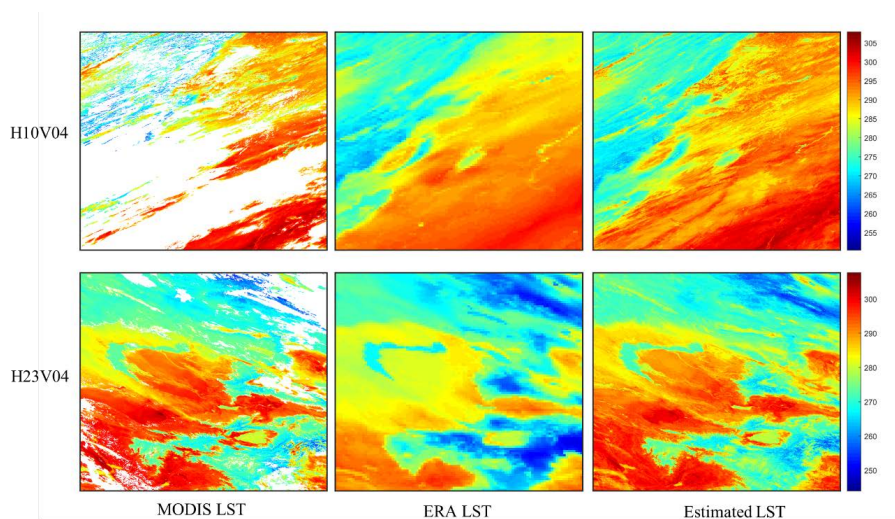
Fig. 13 Spatial details of the MODIS LST, ERA LST and estimated instantaneous LST of two tiles, H10V04 (the first row) and

H23V04 (second row) from the ninetieth day in 2010

536

537

Fig. 14 Spatial details of the daily mean LST retrieved from MODIS LST, ERA LST and estimated daily mean LST of two tiles

H10V04 (first row) and H23V04 (second row) from the ninetieth day in 2010.

In addition, Fig. 15 and Fig. 16 show the estimated instantaneous and daily mean LST at the global

scale on Days 90 and 270 of 2010. The instantaneous and daily mean LST from MODIS LST are shown

for comparison. The estimated instantaneous and daily LST had similar spatial patterns to the

corresponding LST from MODIS. All of the results reflected broad spatiotemporal variations. For

instance, LSTs were relatively higher at middle and low latitudes, and lower in the Arctic and Antarctic.

545   The instantaneous LST exhibited a larger range than the daily mean LST. In addition, the proposed

546   method achieved the all-weather LST retrievals. For instantaneous LST (Fig. 15), a small number of gaps

547   in tropical regions were due to the polar-orbiting satellite configuration. The daily mean LST (Fig. 16)

548   was spatially continuous. Overall, the proposed instantaneous LST and daily mean LST perform well on

549   a global scale.
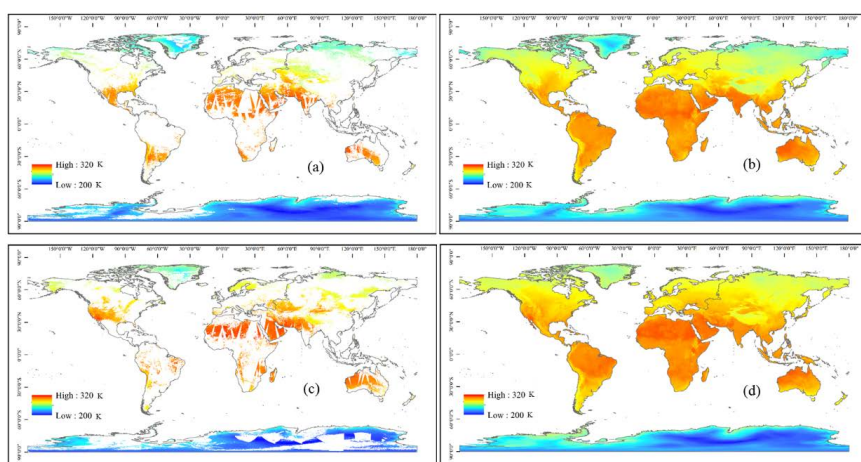
550
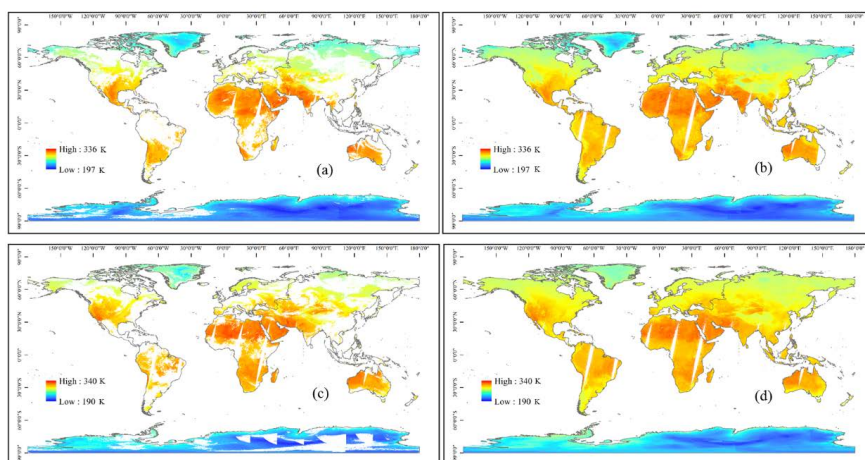
552   Fig. 15 Spatial patterns of MODIS LST (a, c) and estimated instantaneous LST (b, d) at a global scale on the Days 90 (first row)

553   and 270 (second row) of 2010.

555   Fig. 16 Spatial patterns of daily mean LST retrieved from (a, c) MODIS LST and (b, d) estimated daily mean LST at a

556   global scale on Days 90 (first row) and 270 (second row) of 2010.

557

5 Discussion

558

559 Although several LST satellite products have been published, they are missing data under cloudy-

560 sky conditions. Existing research on all-weather LST has mostly been conducted at the regional scale.

561 This study proposes a highly accurate and efficient algorithm to retrieve all-weather LST at a global scale

562 from multi-source data, including MODIS TOA, surface radiation, reanalysis and in situ data. An all-

563 weather daily mean LST algorithm was also proposed. Both the estimated instantaneous and daily mean

564 LST had acceptable accuracy. In addition, it performs well based on independent ground measurements

565 and space-time verification.

5.1 Effect of introducing MODIS TOA information and ERA LST

566

567 In view of the complexity of global climate conditions, and to include more information to estimate

568 the all-weather LST, we introduced MODIS TOA data on the basis of using surface variables. In addition,

569 since the Global Land Data Assimilation System (GLDAS) LST used in previous studies did not have

570 global coverage (the Antarctica region was missing), we introduced the ERA LST in this study, which

571 not only has global coverage, but also has a higher spatio-temporal resolution (0.1°,1 h). We conducted

572 experiments with combinations of different features, to clarify the effect of introducing MODIS TOA

573 information and ERA LST under different weather conditions. A comparison of the removal of ERA LST

574 and MODIS TOA data in the models is shown in Table 6. The results show that when the ERA LST and

575 TOA data were removed, the accuracy of the model was greatly reduced. The RMSEs increased from

576 2.787 to 3.536 K and 3.466 K when ERA LST and TOA data were removed, respectively. However, the

577 accuracy changes in the two feature combinations under different weather conditions were significantly

578 different. When ERA LST was eliminated, although the accuracies of both weather conditions were

579 reduced, the RMSE increase for cloudy sky (0.95 K) was significantly greater than that for clear sky

580 (0.09 K). When the TOA data was removed, the results were the opposite. The accuracy of clear-sky LST

581 estimation decreased significantly. Overall, introducing MODIS TOA information and ERA LST

582 significantly improved the model accuracy. In addition, it can be inferred that ERA LST provides more

583 effective information for cloudy-sky LST estimation, while TOA data contributes more to clear-sky

584 conditions.

585

586

587   Table 6. The accuracy of the independent dataset with different feature combinations for the instantaneous LST model

Feature combination	All-weather			Clear sky			Cloudy sky		
	RMSE	Bias	R^2	RMSE	Bias	R^2	RMSE	Bias	R^2
All features	2.787	0.178	0.974	2.614	0.082	0.982	2.931	0.240	0.965
No ERA LST	3.536	-0.012	0.959	2.730	-0.14	0.9801	3.95	0.07	0.9409
No Toa data	3.466	0.335	0.960	3.620	0.21	0.9604	3.36	0.41	0.9604

588

5.2 Effect of multiple MODIS observations

590   In contrast to most studies using MODIS data in sinusoidal projection, we used swath-type MODIS

591   data to estimate daily mean LST in this study. MODIS swath data can provide more observations,

592   particularly at high latitudes. Furthermore, we statistically analyzed the relationship between the daily

593   mean LST model error and MODIS observation frequency. Fig. 17 shows that the error decreased with

594   an increase in the MODIS observation frequency. For high-latitude areas with more observations, the

595   model accuracy at high latitudes was improved. This demonstrates the superiority of using MODIS data

596   in swath types with more observations to construct a daily mean LST model.
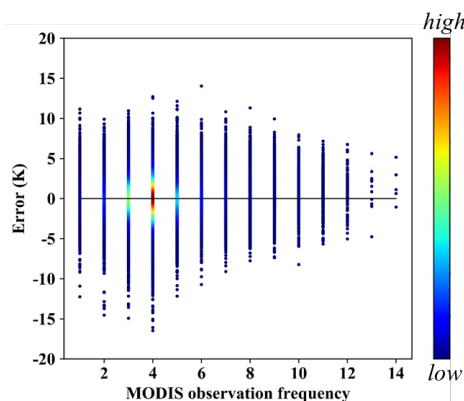
597

598   Fig. 17 Density plots of daily mean LST model error with respect to MODIS observation frequency

5.3 Effect of in situ measurements in the model

600   In contrast to previous studies that used machine learning algorithms, in situ measurements were

601   used to construct the model instead of clear-sky MODIS LST. In situ measurements can obtain the real

602 LST under cloudy-sky conditions, without obtaining the hypothetical LST from clear-sky MODIS LST.

603 In addition, LST from in situ measurements is close to hemispherical LST, or observing the LST from

604 the zenith. In contrast, MODIS LST is a directional LST with view angles ranging from 0° ups to >60°,

605 resulting in a significant thermal radiation directionality (TRD) effect (Cao et al. 2019; Ermida et al.

606 2017). This results in a difference in the LST of the same object at different observation angles.

607 Theoretically, the proposed instantaneous LST weakens the influence of the TRD effect, which was been

608 confirmed in our previous study (Li et al. 2021).

609 **5.4 Effect of the new algorithm on product generation**

610 In previous study, the random forest algorithm (RF) was used to estimate the all-weather LST over

611 the conterminous United States (Li et al. 2021). Although the RF algorithm performs well, the application

612 efficiency needs to be considered for generating global products. Hence, the model accuracy and

613 efficiency were compared using RF and XGBOOST. The model accuracies of RF and XGBOOST was

614 comparable, with RMSEs of 2.787 K and 2.801 K, respectively (Table 7). However, training the

615 XGBOOST model significantly less time, taking up 3.33 minutes compared to 60.01 minutes for RF

616 training. XGBOOST also had outstanding performance in model application. As an example, to produce

617 100 LST swath-type images, the XGBOOST took 8.93 minutes while the RF model took 38.85 minutes

618 (Table 7). Considering the quantities of swath files at the global scale, XGBOOST is a better choice for

619 long-sequence product generation, with high accuracy and efficiency.

620

Table 7 Comparison of algorithms of model accuracy and efficiency.

Algorithm	Model accuracy			Model efficiency	
	RMSE (K)	Bias (K)	R^2	Training time(minute)	Application time (minute)
XGBOOST	2.787	0.178	0.974	3.33	8.93
RF	2.801	0.196	0.974	60.01	38.85

621

622 **5.5 Limitations**

623 However, this study has certain limitations. Despite enhancements in LST accuracy on ice and snow

624 surfaces, accuracy remains comparatively lower in barren and urban areas. Additionally, while the study

625 aimed to select the highest possible number of representative ground stations for the long-term sequence,

626 the spatial distribution was non-uniform, potentially impacting the generality of data-driven models.

627   Furthermore, the accuracy of the high-altitude model was marginally lower, possibly attributed to the

628   complex climatic environment and topographic conditions. Future investigations could employ advanced

629   methods, such as deep learning, to develop a more adaptive model incorporating spatial and temporal

630   information. Moreover, integration with other satellite sensors has the potential to extend the temporal-

631   spatial resolution and time span of all-weather LST products.

632

6 Data availability

633

634   The global all-weather LST data at monthly scale from 2000-2020 can be freely downloaded from

635   https://doi.org/10.5281/zenodo.4292068(Li et al. 2024), the daily mean LST on the first day of year 2010

636   is freely available at https://doi.org/10.5281/zenodo.4292068(Li et al. 2024), all the data will be available

637   at https://glass-product.bnu.edu.cn/dload.html.

638

639 **7 Conclusion**

640   LST is a crucial parameter of the Earth's energy budget, and current LST satellite products are

641 affected by cloud contamination, resulting in missing values. This study attempted to retrieve all-weather

642 instantaneous and daily mean LST at a global scale. A new framework that generating global, long-

643 sequence LST product is proposed. Multiple all-weather datasets from MODIS TOA observations,

644 surface radiation data, geolocation data, reanalysis data, and ground measurements were used to construct

645 the models.

646   Based on the XGBOOST algorithm and multisource data from 2002-2018, all-weather

647 instantaneous and daily mean LST models were successively built. The validation of the independent

648 dataset showed high accuracy. The ten-fold cross validation demonstrated the robustness of the models.

649 For the instantaneous LST model, clear-sky LST showed higher accuracy than cloudy-sky LST, while

650 cloud contamination had limited effects on daily mean LST estimations. Both models performed well for

651 most land cover types and geolocation conditions. The time series for validation at the four sites from

652 different regions was temporally contiguous. The results showed high consistency with in situ

653 measurements and the corresponding official MODIS LST. The spatial distributions of MODIS tiles

654 showed more spatial details than the ERA LST. Global mapping illustrated spatial continuity and similar

655 patterns with instantaneous and daily mean LST from the official MODIS LST data.

656   Compared with previous products, adding TOA observations effectively improved the accuracy of

657 the instantaneous model, especially under clear-sky conditions. Moreover, multiple effective swath-type

658 observations from the MODIS data significantly improved the accuracy of the daily mean LST model.

659 In contrast to the MODIS and ERA LST, the proposed all-weather method has a higher accuracy and is

660 less affected by cloud contamination, especially at high latitudes. In terms of product generation,

661 XGBOOST has higher precision and efficiency compared with RF, and provides effective support for

662 mass data production.

663   Overall, the proposed models were effective and robust, demonstrating the potential of estimating

664 all-weather instantaneous and daily mean LST from multisource data. The constructed models can be

665 used to generate long-sequence LST products from 2000 to present. The generated product is a 1 km all-

666 weather instantaneous and daily mean LST products at a global scale. It has great significance for studies

667 on climate change, surface energy balance, and many other scientific fields. In the future, new methods

668   involving spatial and temporal information, as well as other satellite sensors, should be considered to

669   expand the spatiotemporal monitoring capabilities of LST products.

670

671 **Declaration of Competing Interest**

672 Author Han Ma is a member of the editorial board of the journal.

673

685   **Reference**

686   Aires, F., Prigent, C., & Rossow, W.B. (2004). Temporal interpolation of global
687   surface skin temperature diurnal cycle over land under clear and cloudy conditions.
688   *Journal of Geophysical Research: Atmospheres, 109*, 313-331

689   Baldocchi, D., Falge, E., Gu, L., Olson, R., Hollinger, D., Running, S., Anthoni,
690   P., Bernhofer, C., Davis, K., Evans, R., Fuentes, J., Goldstein, A., Katul, G., Law, B.,
691   Lee, X., Malhi, Y., Meyers, T., Munger, W., Oechel, W., Paw, K.T., Pilegaard, K.,
692   Schmid, H.P., Valentini, R., Verma, S., Vesala, T., Wilson, K., & Wofsy, S. (2001).
693   FLUXNET: A New Tool to Study the Temporal and Spatial Variability of Ecosystem–
694   Scale Carbon Dioxide, Water Vapor, and Energy Flux Densities. *Bulletin of the
695   American Meteorological Society, 82*, 2415-2434

696   Baldocchi, D.D. (2003). Assessing the eddy covariance technique for evaluating
697   carbon dioxide exchange rates of ecosystems: past, present and future. *Glob Chang Biol,
698   9*, 479-492

699   Bastiaanssen, W.G., Menenti, M., Feddes, R., & Holtslag, A. (1998). A remote
700   sensing surface energy balance algorithm for land (SEBAL). 1. Formulation. *Journal
701   of Hydrology, 212*, 198-212

702   Boden, T.A., Krassovski, M., & Yang, B. (2013). The AmeriFlux data activity and
703   data system: an evolving collection of data management techniques, tools, products and
704   services. *Geoscientific Instrumentation, Methods and Data Systems, 2*, 165-176

705   Breiman, L. (2001). Random forests. *Machine Learning, 45*, 5-32

706   Cao, B., Liu, Q., Du, Y., Roujean, J.-L., Gastellu-Etchegorry, J.-P., Trigo, I.F., Zhan,
707   W., Yu, Y., Cheng, J., Jacob, F., Lagouarde, J.-P., Bian, Z., Li, H., Hu, T., & Xiao, Q.
708   (2019). A review of earth surface thermal radiation directionality observing and
709   modeling: Historical development, current status and perspectives. *Remote Sensing of
710   Environment, 232*

711   Chen, B., Huang, B., & Xu, B. (2015). Comparison of Spatiotemporal Fusion
712   Models: A Review. *Remote Sensing, 7*, 1798-1835

713   Chen, T., & Guestrin, C. (2016). Xgboost: A scalable tree boosting system. In,
714   *Proceedings of the 22nd acm sigkdd international conference on knowledge discovery
715   and data mining* (pp. 785-794)

716   Chen, Y., Liang, S., Ma, H., Li, B., He, T., & Wang, Q. (2021). An all-sky 1 km
717   daily surface air temperature product over mainland China for 2003–2019 from MODIS
718   and ancillary data. *Earth System Science Data*

719   Cheng, J., & Liang, S. (2013). Estimating global land surface broadband thermal-
720   infrared emissivity using advanced very high resolution radiometer optical data.
721   *International Journal of Digital Earth, 6*, 34-49

722   Cheng, J., & Liang, S. (2014). Estimating the broadband longwave emissivity of
723   global bare soil from the MODIS shortwave albedo product. *Journal of Geophysical
724   Research: Atmospheres, 119*, 614-634

725   Cheng, J., & Liang, S. (2016). Global Estimates for High-Spatial-Resolution
726   Clear-Sky Land Surface Upwelling Longwave Radiation From MODIS Data. *IEEE
727   Transactions on Geoscience and Remote Sensing, 54*, 4115-4129

728   Cheng, J., Liang, S., Wang, W., & Guo, Y. (2017). An efficient hybrid method for

729 estimating clear-sky surface downward longwave radiation from MODIS data. *Journal*
730 *of Geophysical Research: Atmospheres, 122*, 2616-2630

731 De Jeu, R.A. (2003). Retrieval of land surface parameters using passive
732 microwave remote sensing. *PhD diss., Vrije Universiteit Amsterdam*

733 Driemel, A., Augustine, J., Behrens, K., Colle, S., Cox, C., Cuevas-Agulló, E.,
734 Denn, F.M., Duprat, T., Fukuda, M., Grobe, H., Haeffelin, M., Hodges, G., Hyett, N.,
735 Ijima, O., Kallis, A., Knap, W., Kustov, V., Long, C.N., Longenecker, D., Lupi, A.,
736 Maturilli, M., Mimouni, M., Ntsangwane, L., Ogihara, H., Olano, X., Olefs, M., Omori,
737 M., Passamani, L., Pereira, E.B., Schmithüsen, H., Schumacher, S., Sieger, R., Tamlyn,
738 J., Vogt, R., Vuilleumier, L., Xia, X., Ohmura, A., & König-Langlo, G. (2018). Baseline
739 Surface Radiation Network (BSRN): structure and data description (1992–2017). *Earth*
740 *System Science Data, 10*, 1491-1501

741 Duan, S.-B., Li, Z.-L., Cheng, J., & Leng, P. (2017a). Cross-satellite comparison
742 of operational land surface temperature products derived from MODIS and ASTER
743 data over bare soil surfaces. *Isprs Journal of Photogrammetry and Remote Sensing, 126*,
744 1-10

745 Duan, S.-B., Li, Z.-L., & Leng, P. (2017b). A framework for the retrieval of all-
746 weather land surface temperature at a high spatial resolution from polar-orbiting
747 thermal infrared and passive microwave data. *Remote Sensing of Environment, 195*,
748 107-117

749 Duan, S.-B., Li, Z.-L., Tang, B.-H., Wu, H., Tang, R., Bi, Y., & Zhou, G. (2014).
750 Estimation of Diurnal Cycle of Land Surface Temperature at High Temporal and Spatial
751 Resolution from Clear-Sky MODIS Data. *Remote Sensing, 6*, 3247-3262

752 Duan, S.-B., Li, Z.-L., Wang, N., Wu, H., & Tang, B.-H. (2012). Evaluation of six
753 land-surface diurnal temperature cycle models using clear-sky in situ and satellite data.
754 *Remote Sensing of Environment, 124*, 15-25

755 Ermida, S.L., DaCamara, C.C., Trigo, I.F., Pires, A.C., Ghent, D., & Remedios, J.
756 (2017). Modelling directional effects on remotely sensed land surface temperature.
757 *Remote Sensing of Environment, 190*, 56-69

758 He, L., Cheng, Y., Li, Y., Li, F., Fan, K., & Li, Y. (2021). An Improved Method for
759 Soil Moisture Monitoring With Ensemble Learning Methods Over the Tibetan Plateau.
760 *IEEE Journal of Selected Topics in Applied Earth Observations and Remote Sensing,*
761 *14*, 2833-2844

762 Hersbach, H., Bell, B., Berrisford, P., Hirahara, S., Horányi, A., Muñoz-Sabater,
763 J., Nicolas, J., Peubey, C., Radu, R., Schepers, D., Simmons, A., Soci, C., Abdalla, S.,
764 Abellan, X., Balsamo, G., Bechtold, P., Biavati, G., Bidlot, J., Bonavita, M., Chiara, G.,
765 Dahlgren, P., Dee, D., Diamantakis, M., Dragani, R., Flemming, J., Forbes, R., Fuentes,
766 M., Geer, A., Haimberger, L., Healy, S., Hogan, R.J., Hólm, E., Janisková, M., Keeley,
767 S., Laloyaux, P., Lopez, P., Lupu, C., Radnoti, G., Rosnay, P., Rozum, I., Vamborg, F.,
768 Villaume, S., & Thépaut, J.N. (2020). The ERA5 global reanalysis. *Quarterly Journal*
769 *of the Royal Meteorological Society, 146*, 1999-2049

770 Holmes, T.R.H., De Jeu, R.A.M., Owe, M., & Dolman, A.J. (2009). Land surface
771 temperature from Ka band (37 GHz) passive microwave observations. *Journal of*
772 *Geophysical Research, 114*

773   Hong, F., Zhan, W., Göttsche, F.-M., Lai, J., Liu, Z., Hu, L., Fu, P., Huang, F., Li,
774   J., Li, H., & Wu, H. (2021). A simple yet robust framework to estimate accurate daily
775   mean land surface temperature from thermal observations of tandem polar orbiters.
776   *Remote Sensing of Environment, 264*, 112612

777   Hong, F., Zhan, W., Göttsche, F.-M., Liu, Z., Dong, P., Fu, H., Huang, F., & Zhang,
778   X. (2022). A global dataset of spatiotemporally seamless daily mean land surface
779   temperatures: generation, validation, and analysis. *Earth System Science Data, 14*,
780   3091-3113

781   Inamdar, A.K., French, A., Hook, S., Vaughan, G., & Luckett, W. (2008). Land
782   surface temperature retrieval at high spatial and temporal resolutions over the
783   southwestern United States. *Journal of Geophysical Research, 113*

784   Jia, A., Ma, H., Liang, S., & Wang, D. (2021). Cloudy-sky land surface
785   temperature from VIIRS and MODIS satellite data using a surface energy balance-
786   based method. *Remote Sensing of Environment, 263*, 112566

787   Jin, M., & Dickinson, R.E. (2000). A generalized algorithm for retrieving cloudy
788   sky skin temperature from satellite thermal infrared radiances. *Journal of Geophysical
789   Research: Atmospheres, 105*, 27037-27047

790   Kalma, J.D., McVicar, T.R., & McCabe, M.F. (2008). Estimating land surface
791   evaporation: A review of methods using remotely sensed surface temperature data.
792   *Surveys in Geophysics, 29*, 421-469

793   Kappas, M., & Phan, T.N. (2018). Application of MODIS land surface temperature
794   data: a systematic literature review and analysis. *Journal of Applied Remote Sensing,
795   12*, 1

796   Kim, M., Brunner, D., & Kuhlmann, G. (2021). Importance of satellite
797   observations for high-resolution mapping of near-surface NO2 by machine learning.
798   *Remote Sensing of Environment, 264*, 112573

799   Lawrimore, J.H., Menne, M.J., Gleason, B.E., Williams, C.N., Wuertz, D.B., Vose,
800   R.S., & Rennie, J. (2011). An overview of the Global Historical Climatology Network
801   monthly mean temperature data set, version 3. *Journal of Geophysical Research, 116*

802   Li, B., Liang, S., Liu, X., Ma, H., Chen, Y., Liang, T., & He, T. (2021). Estimation
803   of all-sky 1 km land surface temperature over the conterminous United States. *Remote
804   Sensing of Environment, 266*, 112707

805   Li, B., Liang, S., Ma, H., Liu, X., He, T., & Zhang, Y. (2024). All-weather 1km
806   land surface temperature at global scale from 2000-2020 from MODIS data.Zenodo
807   [Data set]. Zenodo. https://doi.org/10.5281/zenodo.4292068

808   Li, J.-H., Li, Z.-L., Liu, X., Duan, S.-B., Si, M., Shang, G., & Zhang, X. (2023). A
809   generalized method for retrieving global daily mean land surface temperature from
810   polar-orbiting thermal infrared sensor instantaneous observations. *International
811   Journal of Remote Sensing*, 1-22

812   Li, Z.-L., Tang, B.-H., Wu, H., Ren, H., Yan, G., Wan, Z., Trigo, I.F., & Sobrino,
813   J.A. (2013). Satellite-derived land surface temperature: Current status and perspectives.
814   *Remote Sensing of Environment, 131*, 14-37

815   Liang, S., Cheng, J., Jia, K., Jiang, B., Liu, Q., Xiao, Z., Yao, Y., Yuan, W., Zhang,
816   X., Zhao, X., & Zhou, J. (2021). The Global Land Surface Satellite (GLASS) Product

817 Suite. *Bulletin of the American Meteorological Society, 102*, E323-E337

818 Liang, S., Zhang, X., Xiao, Z., Cheng, J., Liu, Q., & Zhao, X. (2013a). *Global
819 LAnd Surface Satellite (GLASS) products: algorithms, validation and analysis.*
820 Springer Science & Business Media

821 Liang, S., Zhao, X., Liu, S., Yuan, W., Cheng, X., Xiao, Z., Zhang, X., Liu, Q.,
822 Cheng, J., Tang, H., Qu, Y., Bo, Y., Qu, Y., Ren, H., Yu, K., & Townshend, J. (2013b).
823 A long-term Global LAnd Surface Satellite (GLASS) data-set for environmental studies.
824 *International Journal of Digital Earth, 6*, 5-33

825 Liu, Q., Wang, L., Qu, Y., Liu, N., Liu, S., Tang, H., & Liang, S. (2013a).
826 Preliminary evaluation of the long-term GLASS albedo product. *International Journal
827 of Digital Earth, 6*, 69-95

828 Liu, S., Li, X., Xu, Z., Che, T., Xiao, Q., Ma, M., Liu, Q., Jin, R., Guo, J., Wang,
829 L., Wang, W., Qi, Y., Li, H., Xu, T., Ran, Y., Hu, X., Shi, S., Zhu, Z., Tan, J., Zhang, Y.,
830 & Ren, Z. (2018). The Heihe Integrated Observatory Network: A Basin-Scale Land
831 Surface Processes Observatory in China. *Vadose Zone Journal, 17*, 180072

832 Liu, S.M., Xu, Z.W., Zhu, Z.L., Jia, Z.Z., & Zhu, M.J. (2013b). Measurements of
833 evapotranspiration from eddy-covariance systems and large aperture scintillometers in
834 the Hai River Basin, China. *Journal of Hydrology, 487*, 24-38

835 Liu, X., Liang, S., Li, B., Ma, H., & He, T. (2021). Mapping 30 m Fractional Forest
836 Cover over China's Three-North Region from Landsat-8 Data Using Ensemble
837 Machine Learning Methods. *Remote Sensing, 13*, 2592

838 Liu, Y., Ackerman, S.A., Maddux, B.C., Key, J.R., & Frey, R.A. (2010). Errors in
839 Cloud Detection over the Arctic Using a Satellite Imager and Implications for
840 Observing Feedback Mechanisms. *Journal of Climate, 23*, 1894-1907

841 Long, D., Yan, L., Bai, L., Zhang, C., Li, X., Lei, H., Yang, H., Tian, F., Zeng, C.,
842 Meng, X., & Shi, C. (2020). Generation of MODIS-like land surface temperatures
843 under all-weather conditions based on a data fusion approach. *Remote Sensing of
844 Environment, 246*

845 Lu, L., Venus, V., Skidmore, A., Wang, T., & Luo, G. (2011). Estimating land-
846 surface temperature under clouds using MSG/SEVIRI observations. *International
847 Journal of Applied Earth Observation and Geoinformation, 13*, 265-276

848 Ma, L., Liu, Y., Zhang, X., Ye, Y., Yin, G., & Johnson, B.A. (2019). Deep learning
849 in remote sensing applications: A meta-analysis and review. *Isprs Journal of
850 Photogrammetry and Remote Sensing, 152*, 166-177

851 Ma, Y., Hu, Z., Xie, Z., Ma, W., Wang, B., Chen, X., Li, M., Zhong, L., Sun, F.,
852 Gu, L., Han, C., Zhang, L., Liu, X., Ding, Z., Sun, G., Wang, S., Wang, Y., & Wang, Z.
853 (2020). A long-term (2005–2016) dataset of hourly integrated land–atmosphere
854 interaction observations on the Tibetan Plateau. *Earth Syst. Sci. Data, 12*, 2937-2957

855 Mao, K., Shi, J., Li, Z., Qin, Z., Li, M., & Xu, B. (2007). A physics-based statistical
856 algorithm for retrieving land surface temperature from AMSR-E passive microwave
857 data. *Science in China Series D: Earth Sciences, 50*, 1115-1120

858 Mao, K., Zuo, Z., Shen, X., Xu, T., Gao, C., & Liu, G. (2018). Retrieval of Land-
859 surface Temperature from AMSR2 Data Using a Deep Dynamic Learning Neural
860 Network. *Chinese Geographical Science, 28*, 1-11

861 McFarland, M.J., Miller, R.L., & Neale, C.M.U. (1990). Land surface temperature
862 derived from the SSM/I passive microwave brightness temperatures. *IEEE*
863 *Transactions on Geoscience and Remote Sensing, 28*, 839-845

864 Mercury, M., Green, R., Hook, S., Oaida, B., Wu, W., Gunderson, A., & Chodas,
865 M. (2012). Global cloud cover for assessment of optical satellite observation
866 opportunities: A HyspIRI case study. *Remote Sensing of Environment, 126*, 62-71

867 Metz, M., Rocchini, D., & Neteler, M. (2014). Surface Temperatures at the
868 Continental Scale: Tracking Changes with Remote Sensing at Unprecedented Detail.
869 *Remote Sensing, 6*, 3822-3840

870 Muñoz-Sabater, J., Dutra, E., Agustí-Panareda, A., Albergel, C., Arduini, G.,
871 Balsamo, G., Boussetta, S., Choulga, M., Harrigan, S., Hersbach, H., Martens, B.,
872 Miralles, D.G., Piles, M., Rodríguez-Fernández, N.J., Zsoter, E., Buontempo, C., &
873 Thépaut, J.-N. (2021). ERA5-Land: a state-of-the-art global reanalysis dataset for land
874 applications. *Earth System Science Data, 13*, 4349-4383

875 Ohmura, A., Gilgen, H., Hegner, H., Müller, G., Wild, M., Dutton, E.G., Forgan,
876 B., Fröhlich, C., Philipona, R., Heimo, A., König-Langlo, G., McArthur, B., Pinker, R.,
877 Whitlock, C.H., & Dehne, K. (1998). Baseline Surface Radiation Network
878 (BSRN/WCRP): New Precision Radiometry for Climate Research. *Bulletin of the*
879 *American Meteorological Society, 79*, 2115-2136

880 Østby, T.I., Schuler, T.V., & Westermann, S. (2014). Severe cloud contamination
881 of MODIS Land Surface Temperatures over an Arctic ice cap, Svalbard. *Remote*
882 *Sensing of Environment, 142*, 95-102

883 Pede, T., & Mountrakis, G. (2018). An empirical comparison of interpolation
884 methods for MODIS 8-day land surface temperature composites across the
885 conterminous Unites States. *Isprs Journal of Photogrammetry and Remote Sensing, 142*,
886 137-150

887 Qu, Y., Liang, S., Liu, Q., Li, X., Feng, Y., & Liu, S. (2016). Estimating Arctic sea-
888 ice shortwave albedo from MODIS data. *Remote Sensing of Environment, 186*, 32-46

889 Qu, Y., Liu, Q., Liang, S., Wang, L., Liu, N., & Liu, S. (2014). Direct-Estimation
890 Algorithm for Mapping Daily Land-Surface Broadband Albedo From MODIS Data.
891 *IEEE Transactions on Geoscience and Remote Sensing, 52*, 907-919

892 Rao, Y., Liang, S., Wang, D., Yu, Y., Song, Z., Zhou, Y., Shen, M., & Xu, B. (2019).
893 Estimating daily average surface air temperature using satellite land surface
894 temperature and top-of-atmosphere radiation products over the Tibetan Plateau. *Remote*
895 *Sensing of Environment, 234*, 111462

896 Shen, H., Jiang, Y., Li, T., Cheng, Q., Zeng, C., & Zhang, L. (2020). Deep learning-
897 based air temperature mapping by fusing remote sensing, station, simulation and
898 socioeconomic data. *Remote Sensing of Environment, 240*

899 Shiff, S., Helman, D., & Lensky, I.M. (2021). Worldwide continuous gap-filled
900 MODIS land surface temperature dataset. *Sci Data, 8*, 74

901 Stokes, G.M., & Schwartz, S.E. (1994). The Atmospheric Radiation Measurement
902 (ARM) Program: Programmatic Background and Design of the Cloud and Radiation
903 Test Bed. *Bulletin of the American Meteorological Society, 75*, 1201-1221

904 Sun, D., & Pinker, R.T. (2005). Implementation of GOES-based land surface

905 temperature diurnal cycle to AVHRR. *International Journal of Remote Sensing, 26*,
906 3975-3984

907 Tomlinson, C.J., Chapman, L., Thornes, J.E., & Baker, C. (2011). Remote sensing
908 land surface temperature for meteorology and climatology: a review. *Meteorological*
909 *Applications, 18*, 296-306

910 Townshend, J.R.G., Justice, C.O., Skole, D., Malingreau, J.P., Cihlar, J., Teillet, P.,
911 Sadowski, F., & Ruttenberg, S. (2007). The 1 km resolution global data set: needs of
912 the International Geosphere Biosphere Programme†. *International Journal of Remote*
913 *Sensing, 15*, 3417-3441

914 Wan, Z. (2014). New refinements and validation of the collection-6 MODIS land-
915 surface temperature/emissivity product. *Remote Sensing of Environment, 140*, 36-45

916 Wan, Z., & Li, Z.-L. (1997). A physics-based algorithm for retrieving land-surface
917 emissivity and temperature from EOS/MODIS data. *IEEE Transactions on Geoscience*
918 *and Remote Sensing, 35*, 980-996

919 Wan, Z., Wang, P., & Li, X. (2010). Using MODIS Land Surface Temperature and
920 Normalized Difference Vegetation Index products for monitoring drought in the
921 southern Great Plains, USA. *International Journal of Remote Sensing, 25*, 61-72

922 Wang, N., Tang, B.-H., Li, C., & Li, Z.-L. (2010). A generalized neural network
923 for simultaneous retrieval of atmospheric profiles and surface temperature from
924 hyperspectral thermal infrared data, 1055-1058

925 Weng, Q. (2009). Thermal infrared remote sensing for urban climate and
926 environmental studies: Methods, applications, and trends. *Isprs Journal of*
927 *Photogrammetry and Remote Sensing, 64*, 335-344

928 Williamson, S., Hik, D., Gamon, J., Kavanaugh, J., & Flowers, G. (2014).
929 Estimating Temperature Fields from MODIS Land Surface Temperature and Air
930 Temperature Observations in a Sub-Arctic Alpine Environment. *Remote Sensing, 6*,
931 946-963

932 Wu, P., Su, Y., Duan, S.-b., Li, X., Yang, H., Zeng, C., Ma, X., Wu, Y., & Shen, H.
933 (2022). A two-step deep learning framework for mapping gapless all-weather land
934 surface temperature using thermal infrared and passive microwave data. *Remote*
935 *Sensing of Environment, 277*

936 Wu, P., Yin, Z., Zeng, C., Duan, S., Gottsche, F.-M., Ma, X., Li, X., Yang, H., &
937 Shen, H. (2019). Spatially Continuous and High-resolution Land Surface Temperature:
938 A Review of Reconstruction and Spatiotemporal Fusion Techniques. *arXiv preprint*
939 *arXiv:1909.09316*

940 Xing, Z., Li, Z.-L., Duan, S.-B., Liu, X., Zheng, X., Leng, P., Gao, M., Zhang, X.,
941 & Shang, G. (2021). Estimation of daily mean land surface temperature at global scale
942 using pairs of daytime and nighttime MODIS instantaneous observations. *Isprs Journal*
943 *of Photogrammetry and Remote Sensing, 178*, 51-67

944 Xu, S., & Cheng, J. (2021). A new land surface temperature fusion strategy based
945 on cumulative distribution function matching and multiresolution Kalman filtering.
946 *Remote Sensing of Environment, 254*, 112256

947 Yamamoto, S. (2005). Findings through the AsiaFlux network and a view toward
948 the future. *Journal of Geographical Sciences, 15*, 142

949   Yao, R., Wang, L., Huang, X., Cao, Q., Wei, J., He, P., Wang, S., & Wang, L. (2023).
950   Global seamless and high-resolution temperature dataset (GSHTD), 2001–2020.
951   *Remote Sensing of Environment, 286*

952   Yao, Y., Liang, S., Qin, Q., Wang, K., Liu, S., & Zhao, S. (2012). Satellite detection
953   of increases in global land surface evapotranspiration during 1984-2007. *International
954   Journal of Digital Earth, 5*, 299-318

955   Yu, P., Zhao, T., Shi, J., Ran, Y., Jia, L., Ji, D., & Xue, H. (2022). Global
956   spatiotemporally continuous MODIS land surface temperature dataset. *Sci Data, 9*, 143

957   Yu, W., Ma, M., Wang, X., & Tan, J. (2014). Estimating the land-surface
958   temperature of pixels covered by clouds in MODIS products. *Journal of Applied
959   Remote Sensing, 8*, 083525

960   Yuan, Q., Shen, H., Li, T., Li, Z., Li, S., Jiang, Y., Xu, H., Tan, W., Yang, Q., Wang,
961   J., Gao, J., & Zhang, L. (2020). Deep learning in environmental remote sensing:
962   Achievements and challenges. *Remote Sensing of Environment, 241*

963   Zeng, C., Long, D., Shen, H., Wu, P., Cui, Y., & Hong, Y. (2018). A two-step
964   framework for reconstructing remotely sensed land surface temperatures contaminated
965   by cloud. *Isprs Journal of Photogrammetry and Remote Sensing, 141*, 30-45

966   Zhang, D., Tang, R., Tang, B.-H., Wu, H., & Li, Z.-L. (2015). A Simple Method
967   for Soil Moisture Determination From LST–VI Feature Space Using Nonlinear
968   Interpolation Based on Thermal Infrared Remotely Sensed Data. *IEEE Journal of
969   Selected Topics in Applied Earth Observations and Remote Sensing, 8*, 638-648

970   Zhang, Q., Yuan, Q., Zeng, C., Li, X., & Wei, Y. (2018). Missing Data
971   Reconstruction in Remote Sensing Image With a Unified Spatial–Temporal–Spectral
972   Deep Convolutional Neural Network. *IEEE Transactions on Geoscience and Remote
973   Sensing, 56*, 4274-4288

974   Zhang, T., Zhou, Y., Zhu, Z., Li, X., & Asrar, G.R. (2022). A global seamless 1 km
975   resolution daily land surface temperature dataset (2003–2020). *Earth System Science
976   Data, 14*, 651-664

977   Zhang, X., Wang, D., Liu, Q., Yao, Y., Jia, K., He, T., Jiang, B., Wei, Y., Ma, H.,
978   & Zhao, X. (2019). An operational approach for generating the global land surface
979   downward shortwave radiation product from MODIS data. *IEEE Transactions on
980   Geoscience and Remote Sensing, 57*, 4636-4650

981   Zhang, X., Zhou, J., Liang, S., Chai, L., Wang, D., & Liu, J. (2020). Estimation of
982   1-km all-weather remotely sensed land surface temperature based on reconstructed
983   spatial-seamless satellite passive microwave brightness temperature and thermal
984   infrared data. *Isprs Journal of Photogrammetry and Remote Sensing, 167*, 321-344

985   Zhang, X., Zhou, J., Liang, S., & Wang, D. (2021). A practical reanalysis data and
986   thermal infrared remote sensing data merging (RTM) method for reconstruction of a 1-
987   km all-weather land surface temperature. *Remote Sensing of Environment, 260*, 112437

988   Zhao, W., Duan, S.-B., Li, A., & Yin, G. (2019). A practical method for reducing
989   terrain effect on land surface temperature using random forest regression. *Remote
990   Sensing of Environment, 221*, 635-649

991   Zhou, D., Xiao, J., Bonafoni, S., Berger, C., Deilami, K., Zhou, Y., Frolking, S.,
992   Yao, R., Qiao, Z., & Sobrino, J. (2018). Satellite Remote Sensing of Surface Urban

993   Heat Islands: Progress, Challenges, and Perspectives. *Remote Sensing, 11*, 48

994   Zhou, J., Dai, F., Zhang, X., Zhao, S., & Li, M. (2015). Developing a temporally
995   land cover-based look-up table (TL-LUT) method for estimating land surface
996   temperature based on AMSR-E data over the Chinese landmass. *International Journal*
997   *of Applied Earth Observation and Geoinformation, 34*, 35-50

998